

# Topological Photonics (Mini-review)

A. S. Ustinov<sup>+</sup>, A. S. Shorokhov<sup>+</sup>, D. A. Smirnova<sup>\*×1)</sup>

<sup>+</sup>*Faculty of Physics, Lomonosov Moscow State University, 119991 Moscow, Russia*

<sup>\*</sup>*Institute of Applied Physics, Russian Academy of Science, 603950 Nizhny Novgorod, Russia*

<sup>×</sup>*Research School of Physics, Australian National University, Canberra ACT 2601, Australia*

Submitted 4 November 2021

Resubmitted 4 November 2021

Accepted 5 November 2021

Topological insulators, originally discovered in the context of condensed matter physics, have provided a powerful source of inspiration for the design of novel types of photonic crystals and waveguides. It was unveiled that the quantized global characteristics of the band structure and eigenfunctions in the reciprocal space underpin exotic properties of topological materials, such as their abilities to support scattering-resistant wave transport along the edges or boundary surfaces and host robust confined states at corners or hinges. The topological physics brought to the realm of photonics is enriched by non-Hermitian and nonlinear effects and holds special promise for disorder-immune device applications. We review the recent progress in implementing topological states of light in a plethora of platforms, including metacrystals, arrays of microring resonators and optical waveguide lattices, that furthermore bridges to advances in quantum optics and nonlinear nanophotonics.

DOI: 10.1134/S0021364021240012

**Introduction.** Topological photonics has recently emerged as a novel approach to robust waveguiding and routing of light. It exploits engineered photonic structures [1] with the properties analogous to electronic topological insulators [2] (TIs), which are insulating in their bulk but exhibit conducting states at the surfaces.

The discovered in 1980 quantum Hall (QH) phase, which arises in two-dimensional electron gases under a strong external out-of-plane magnetic field applied, represents the first notable example of the topological insulating phase with broken time-reversal (TR) symmetry [3]. Such materials are distinguished by bulk band gaps in their band structures but support chiral edge states, which propagate unidirectionally along the boundaries with built-in immunity to backscattering from disorder. In 2005, it was shown that strong spin-orbit coupling may imitate the effect of a magnetic field in time-reversal invariant electronic systems, giving rise to the quantum spin-Hall phase [4]. Its simplest form constitutes essentially two copies of the QH phase, where up and down spin electrons are decoupled and experience opposite effective magnetic fields.

The concepts of topology in physics originate in seminal works of Thouless et al. [5, 6] connecting the exper-

imentally observable quantized Hall conductance with the so-called topological invariant, namely, the Chern number, defined in the momentum space. Later it became clear that topological phases are not limited to fermionic systems and can be translated to classical wave phenomena. Unusual manifestations inherent to topologically nontrivial states, including the ability of edge modes to overcome structural imperfections without back-reflection, drive general interest in topological effects within photonics and optical communications [7, 8].

**Basic concepts.** Topological effects in condensed matter systems arise from the presence of topologically distinct energy bands of electron wavefunctions [9]. The band structures can be replicated with electromagnetic waves in periodic media casting analogues of topological insulators in photonics. Topology is a general way of mathematically classifying objects according to their global properties, rather than every small detail. In the narrow sense, this branch of mathematics studies compact surfaces and their characteristics conserved under continuous smooth deformations. The most straightforward example of such topological invariants is the genus, which is the number of holes an object has. Interesting properties of TIs are rooted in wavevector-space topology and the existence of abstract “holes” in the modes of

---

<sup>1)</sup>e-mail: daria.smirnova@anu.edu.au

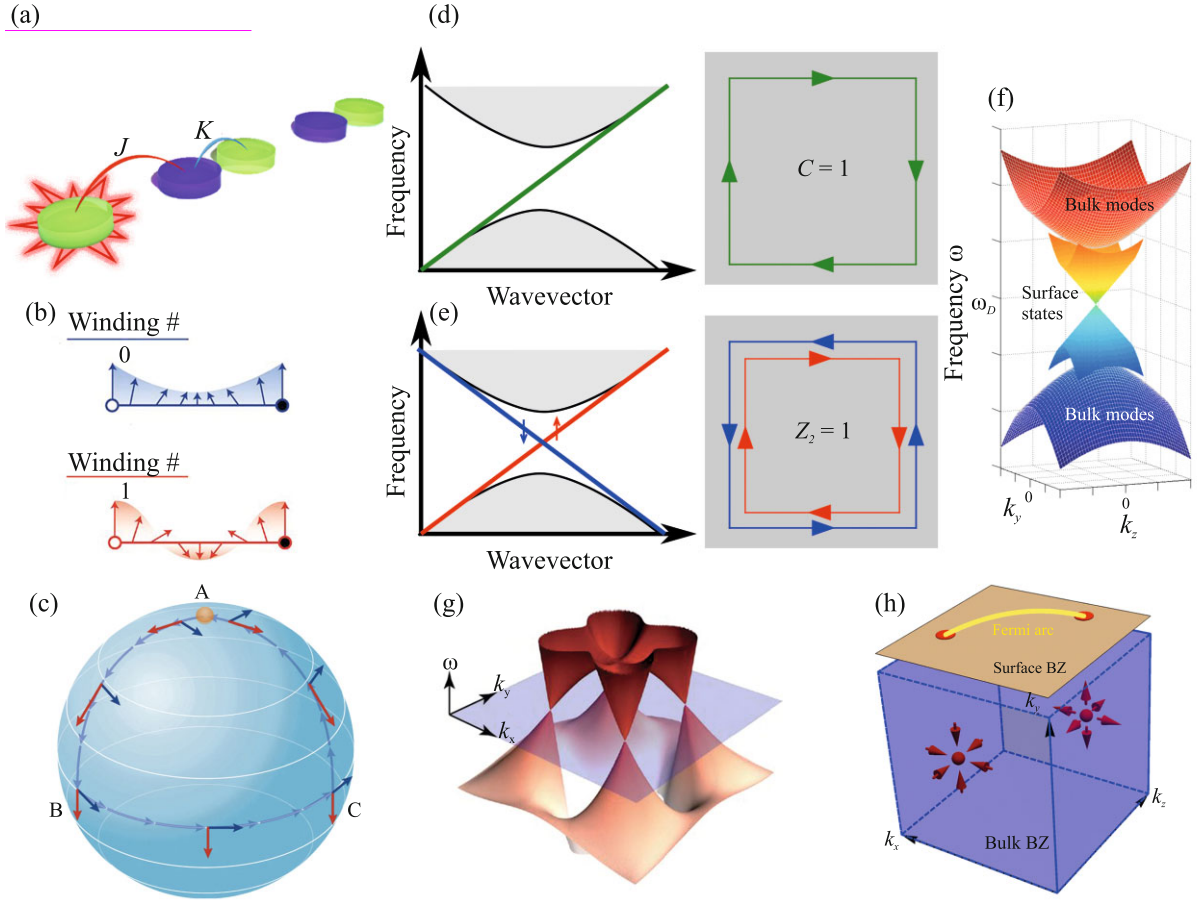


Fig. 1. (Color online) (a) – 1D dimerized array of metaatoms, where  $J$  and  $K$  denote inter- and intradimer hopping strengths, respectively. At  $J \ll K$  the leftmost metaatom supports a strongly localized topological edge state. (b) – Illustration of the winding number with a vector rotary evolution in the 2D Pauli-matrix space, as wave number traverses the Brillouin zone (BZ). (c) – Illustration of a holonomy of vector bundles over the sphere. This property is closely related to the concept of the geometric, or Berry, phase. (d) – Schematic band structure of a finite 2D Chern TI with linearly dispersing chiral edge state. (e) – Schematic band structure of a finite 2D  $Z_2$  TI with spin-polarized edge states crossing the bandgap. Spin-up (down) states are marked with red (blue) arrows. (f) – Schematic band structure of 3D TI. The bulk bands are gapped and the gapless surface states lie within the bulk gap. (g) – Four Weyl points residing on the equi-frequency plane at  $k_z = 0$ . (h) – Schematic of a system with two Weyl points in the 3D bulk Brillouin zone, one of which acts as Berry flux source and the other one as a sink. Adapted from [10–13]

the medium in momentum space. Whenever a material possesses a topological invariant with nonzero value, one can expect physical features that remain insensitive to a range of perturbations. Interfacing two topologically distinct materials results in the formation of peculiar disorder-resistant states at the interface between them, that was recognized as a general principle of the bulk-boundary correspondence.

The simplest lattice that exhibits topological modes is Su-Schrieffer-Heeger (SSH) model, which describes a one-dimensional (1D) dimerized chain with alternating weak and strong couplings between nearest-neighbor sites, see schematic in Fig. 1a. The topological invari-

ant relevant to this model is winding number  $\mathcal{W}$ , which equals 1 if a map of the SSH Hamiltonian to the Pauli matrix space [14–16] is a circle embracing its origin, and thus can be associated with an arrow performing a  $2\pi$ -rotation. By contrast, in the trivial arrangement  $\mathcal{W} = 0$ , and the cyclic evolution of the arrow tip does not show a full rotation, so that the corresponding map can be smoothly contracted into a point in the parametric space (Fig. 1b). The former case corresponds to the SSH chain terminated on a strong bond with a dangling site, that supports a mid-gap staggered edge state exponentially decaying into the bulk.

**Table 1.** Parallels between mathematical and physical quantities in electrodynamics and geometrical band theory [9]

Math	Electrodynamics	Band theory
base space	$\mathbf{r}$ -space sphere	$\mathbf{k}$ -space BZ torus
connection	vector potential $\mathbf{A}(\mathbf{r})$	Berry connection $\mathbf{A}_n(\mathbf{k}) = i\langle u_n   \nabla_{\mathbf{k}} u_n \rangle$
covariant derivative	gauge-invariant momentum $-i\nabla_{\mathbf{r}} + \mathbf{A}(\mathbf{r})$	projected position $i\nabla_{\mathbf{k}} + \mathbf{A}_n(\mathbf{k})$
curvature	magnetic field strength $\mathbf{B} = \nabla_{\mathbf{r}} \times \mathbf{A}(\mathbf{r})$	Berry curvature $\mathbf{\Omega}_n = \nabla_{\mathbf{k}} \times \mathbf{A}_n(\mathbf{k})$
holonomy	Aharonov–Bohm phase $-\oint d\mathbf{r} \cdot \mathbf{A}(\mathbf{r})$	Berry phase $\oint d\mathbf{k} \cdot \mathbf{A}_n(\mathbf{k})$

For arbitrary periodic systems, the topology of a band is determined by both eigenvalues  $\varepsilon_n(\mathbf{k})$  and eigenvectors  $|u_n\rangle$  of the bulk Bloch Hamiltonian as functions of the wave vector  $\mathbf{k}$ . According to notions of topology, in the band theory of solids the parameter space (base manifold) is the Brillouin-zone torus, and the fibers are vector spaces corresponding to per-band subsets of eigenvectors. The linear representation of the structure group  $U(1)$ , playing the role of gauge  $U(1) = \exp(i\varphi)$  in electrodynamics, acts on fibers to produce a fiber bundle over the Brillouin-zone torus. On vector bundles there exists a local gauge-dependent feature called the Berry connection  $\mathbf{A}_n(\mathbf{k})$  closely related to the property of holonomy (Fig. 1c) on smooth surfaces, which allows one to obtain the angle of parallel translation of a vector pinned to a surface along arbitrary path on it; in a similar manner, the former realizes the parallel transport of the vector bundles' sections, the alias for eigenvectors. The Berry connection naturally gives rise to another local characteristic of a vector bundle – the Berry curvature  $\mathbf{\Omega}_n(\mathbf{k}) = \nabla_{\mathbf{k}} \times \mathbf{A}_n(\mathbf{k})$ , continuously defined over the first Brillouin zone. The total flow of the Berry curvature through the surface stretched over the eigenvector evolution contour yields the geometric (Berry) phase, which cannot be eliminated by any gauge transformation of Hamiltonian. These three quantities are the analogues of the vector potential, magnetic field strength, and magnetic flux, respectively (see Table 1). While the Berry connection and curvature contain information about geometric properties of underlying vector bundle, its global topology can only be classified by topological invariants. The simplest illustrative examples of nontrivial fiber bundles include the Möbius band, which is locally indistinguishable of a cylinder but globally differs from it as the the underlying 2D strip is glued with a  $\pi$ -twist, Klein bottle, and Hopf fibration. The cylinder with no twist is a trivial bundle.

The most ubiquitous, in terms of characteristic topological invariants, are the Chern,  $Z_2$  topological insulators, and topological gapless systems with degenerate points or lines, otherwise called topological semimetals.

Chern topological insulators are characterized by the first Chern number. For a particular band, it is defined as an integral of Berry curvature over the first Brillouin zone,  $C_n = \frac{1}{2\pi} \int_{\text{BZ}} d^2\mathbf{k} \mathbf{\Omega}_n(\mathbf{k})$ . The non-zero Chern number implies discontinuity of Berry connection and emergence of the topological charge, which leads to the non-vanishing geometric phase term in a eigenvector. For finite systems, the bulk Chern number accounts for the number of unidirectional topologically protected edge modes [2] (Fig. 1d). In two-dimensional Chern insulators the TR symmetry is necessarily violated, for example, by the magnetic field bias, and in finite Chern TIs the propagation direction of topological edge states is controlled by the sign of the total magnetic flux.

Another class is the  $Z_2$  topological insulators, which can be considered as consisting of two copies of Chern topological insulators with gauge fields acting on opposite spins [2]. Such 2D systems are TR-invariant, and therefore, the Chern number is zero. The topological invariant for this class is defined as  $\nu = (C_{\uparrow} - C_{\downarrow})/2 \bmod 2$  and belongs to the  $Z_2$  additive group of integer numbers, where the Chern numbers  $C_{\uparrow/\downarrow}$  are calculated for the spin up/down subsystems. In the topologically nontrivial case,  $\nu = 1$ , the Kramers partners, time-reversed pairs of eigenstates, can be connected by the odd number of edge modes only, which, being degenerate at  $\mathbf{k} = 0$ , traverse a band gap and cannot be eliminated by any smooth deformation preserving TR symmetry (Fig. 1e). In the topologically trivial case,  $\nu = 0$ , the Kramers partners in the Brillouin zone are connected by pairs of edge states and all of them may thus be pushed into bulk bands.

In fact, it is the TR symmetry that ensures the topological stability of the edge states supported by quantum spin Hall topological insulators, with spin-orbital coupling, in the absence of spin-flipping process. However, one should keep in mind that while TR symmetry alone is sufficient to guarantee the presence of degenerate spin-1/2 states in condensed-matter physics, owing to Kramers' theorem for fermions, this is not the case for photons because they obey the bosonic quantum statistics. Therefore, additional deliberately engineered sym-

metries related to pseudo-time-reversal operators  $\hat{C}_b$ ,  $\hat{C}_b^2 = -1$ ,  $\hat{C}_b \hat{H} \hat{C}_b^{-1} = \hat{H}$  are exploited in photonics to mimic the fermionic property of electrons  $\hat{T}_f^2 = -1$ , with TR operator  $\hat{T}_f = i\hat{\sigma}_y \hat{K}$ , and achieve time-reversal-invariant topological order [7]. They include internal symmetry of the electromagnetic field inside a photonic structure or crystalline symmetries of a photonic lattice. Such symmetries can produce modal degeneracies in a band structure generating doublet states to emulate the pseudospin degree of freedom, thus enabling photonic analogues of the quantum spin-Hall effect [17].

Synthetic gauge fields for light can also be introduced by periodic modulation of photonic crystal parameters in time or space. The effective magnetic field, associated with the complex phase accumulation, can thus force unidirectional propagation of photons without the use of magnetic materials at optical frequencies, in a way similar to electrons moving along skipping orbits along the edge in a two-dimensional magnetically-biased electron gas.

Three-dimensional topological systems include gapped topological insulators [18, 19] hosting surface states with conical dispersion inside the band gap (Fig. 1f), and gapless Weyl semimetals [20, 12] exhibiting linearly dispersing bands at the Weyl points (Fig. 1e, h). Each Weyl point is characterized by the Chern number of the eigenstate bundle over the sphere embracing this point and represents a source or sink of the Berry flux, similar to a magnetic monopole. Importantly, the surface Brillouin zones contain Fermi arcs connecting projections of Weyl sink and source (diabolic) points, see Fig. 1h. Each diabolic point terminates the odd number of surface Fermi arcs [21]. Besides the topologically protected Fermi-arc surface states, photonic Weyl semimetals may enable pronounced Hall effect for photons due to diverging Berry curvature in the vicinity of Weyl points [22]. An optical analog of the ideal three-dimensional Weyl system was demonstrated by Yang et al. using a microwave photonic crystal of saddle-shaped metallic coils [12]. In the ideal Weyl system all the Weyl points rest on the same equi-frequency surface being remote far enough from any other bands (Fig. 1e). Conical dispersion around Weyl points implies the possibilities for efficient manipulation of scattering cross section [23]. Strong light-matter interactions combined with vanishing density of states at Weyl frequencies furthermore suggest opportunities for the emission control of quantum light emitters hybridized with photonic Weyl semimetals.

**2D photonic topological systems.** Figure 2 shows the actual representative demonstrations of

two-dimensional topological photonic systems in their historical sequence.

Following a theoretical proposal by Raghu and Haldane [24–26], Wang et al. were first to realize the photonic counterpart of the quantum Hall effect at microwave frequencies [27]. In their experiment TR symmetry was broken by the magnetic field applied in a square-lattice photonic crystal of gyromagnetic ferrite rods confined vertically between two metallic plates to mimic the TM-polarized modes in infinitely long cylinders (Fig. 2a, b). The resultant band structure hosts a gapless chiral edge state that propagates around defects with back scattering sufficiently significantly suppressed and, by contrast, high transmittance within the band gap shaded yellow in Fig. 2c.

However, the path with preserved TR appears preferential in optics because magneto-optical response is weak at optical frequencies. To create devices compatible with subwavelength optical circuitry, it is more expedient to use semiconductor materials, which are already widely employed in photonics. Time-reversal invariant topological effects were realised in lattices of coupled ring resonators, waveguide arrays, nanophotonic metasurfaces and bianisotropic metamaterials.

A group from Maryland demonstrated topological edge states at near-infrared wavelengths (1.55  $\mu\text{m}$ ) in a two-dimensional square lattice of coupled silicon ring resonators [28] whose diameters are much larger than the wavelength of light (Fig. 2d). Each site ring supports degenerate clockwise and counterclockwise modes, forming a pseudospin degree of freedom, and a gauge field is implemented via differing optical path lengths in auxiliary coupling rings. The link rings are placed asymmetrically between the site rings so that a photon hopping along one direction travels a slightly longer path compared to a photon hopping along the opposite direction. Depending on the pumping direction, two different pseudospins can be excited. The sign of the synthetic magnetic field depends on whether the clockwise or counterclockwise mode is considered. As a result, the observed topological edge state in Fig. 2e propagates around a defect, which does not flip the spin.

Rechtsman et al. implemented a Floquet photonic topological insulator by utilizing spatial modulation along the propagation direction in a honeycomb waveguide array [29]. The diffraction of light in straight laser-written waveguide arrays can be described by the paraxial equation of waveguide mode evolution. Adding an adiabatic helical twist to the waveguides leads to the modified paraxial equation in the transformed coordinate frame that contains the vector potential term. In terms of coupled mode equations, the Peierls substitu-

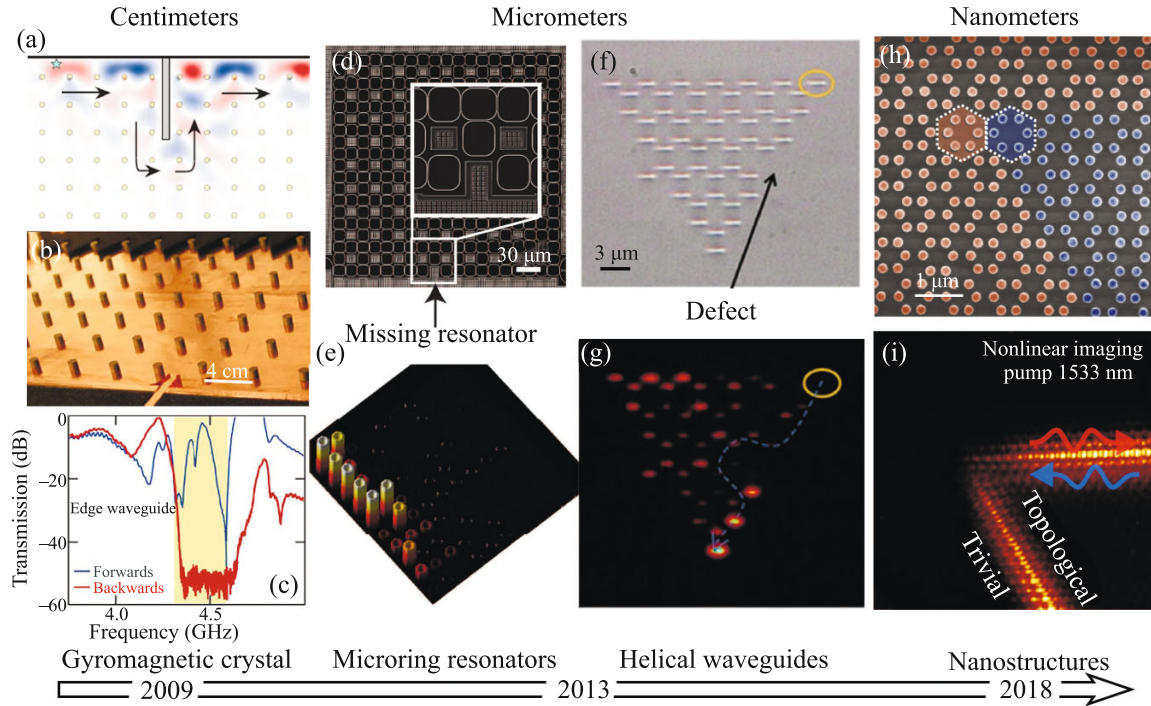


Fig. 2. (Color online) First column: (a) – Demonstration of back- and side-scattering suppression of the edge wave when a large obstacle is inserted in the array of magnetised ferrite rods emulating the quantum Hall topological phase; (b) – Real photograph of the gyromagnetic photonic-crystal slab used in experiment; (c) – Measured spectra confirm unidirectional propagation in the edge waveguide with forward transmission (blue curve) being 50 dB greater than backward transmission (red curve) at mid-gap frequencies. Second column: (d) – A fragment of the topological array of silicon ring resonators with one site-resonator deliberately removed; (e) – Topological protection is experimentally demonstrated as light traverses around the defect. Third column: (f), (g) – A triangle-shaped array of laser-written helical waveguides in glass acts as a photonic topological insulator so that light excited at the corner (yellow circle) is guided along its surface and bypasses a defect, created by a missing waveguide (blue arrow). Fourth column: (h) – A top view of a sample and (i) – Experimental image of the third-harmonic generation from topological edge states in a nanostructured metasurface composed of expanded and shrunken hexamers made of silicon pillars on a glass substrate. Timeline with years is shown on the bottom. Adapted from [27–30]

tion in the presence of a vector potential then yields a phase of the coupling constants between the evanescently coupled nearest-neighbour waveguides. Thereby, a band gap emerges in the Floquet quasi-propagation-constant spectra, which was shown to accommodate a chiral edge state. It was experimentally confirmed that the edge mode excited at the corner waveguide propagates robustly along the array's boundary in one direction with suppressed backscattering from defects, such as acute corners and missing site waveguides (Fig. 2g).

Motivated by optical on-chip applications, the most recent realisations of topological phases in photonics have advanced to the nanoscale. For example, nanophotonic topological modes were designed and imaged via third-harmonic generation by Smirnova et al. in topological arrays of silicon nanopillars [30]. In this metasurface, a topologically nontrivial domain of expanded

hexamers, colored blue in Fig. 2h, is embedded into a trivial domain of shrunken hexamers, colored red, and the frequency conversion is governed by the field localization at the topological domain wall, as shown in Fig. 2i. At the pump wavelengths within the photonic bandgap, the edge states at topological interfaces are spin-momentum locked and bend around corners with suppressed backscattering. By tuning the pump wavelength, it is possible to switch nonlinear light generation between the domains, that directly visualizes band inversion being a signature of nontrivial topology, and observe circular polarization state of the nonlinear diffraction from the metasurface sample in the far field.

**Bianisotropy-based photonic TIs.** Topological states can be designed in artificial metamaterials by employing their bianisotropy. Bianisotropy, also known as magneto-electric coupling, is the property of the par-

particle's polarizability tensor or the material's constitutive relations such that the electric (magnetic) response can be induced by the external magnetic (electric) field. The electromagnetic dual symmetry between electric and magnetic fields can be ensured by the structural design to define pseudospin states, while bianisotropic response is then used to break the degeneracy and introduce an effective spin-orbit coupling. Such bianisotropy in Mie-resonant dielectric particles with overlapped electric and magnetic dipole resonances arises due to the reduced spatial symmetry of the particle's shape [31–36]. It was proposed that metacrystals made of bianisotropic disks can build up a weak 3D photonic TI capable of emulating the relativistic dynamics of massive Dirac fermions and Jackiw–Rebbi states at the interface separating domains with particles of opposite masses [35]. Robust surface states in topological metacrystals can be used for reflectionless routing of electromagnetic energy along arbitrarily shaped paths in 3D space.

In a broader scope, engineering metamaterial properties allows creating synthetic photonic potentials to flexibly control electromagnetic radiation, create cloaked regions, filter and demultiplex light. For instance, combined with another gauge field acting on the valley degree of freedom, bianisotropy enacts the spin-valley-polarized one-way transport [37].

**Higher-order photonic TIs.** Another class of topological systems, higher-order topological insulators, supports gapped boundary states but hosts topological states of lower dimensionality, such as hinge and corner states, as illustrated in Fig. 3a. By analogy to the modern theory of electric polarization [38–40], the higher-order multipole topological insulators are described by higher-order multipole moments inherently quantized by lattice symmetries [42, 41]. Generalizing the bulk-boundary correspondence, the electric quadrupole insulators in the study of Benalcazar et al. [40] do not exhibit gapless edge states but feature mid-gap topological corner excitations. The bulk quadrupole moment induces edge dipole moments and corner charges. In photonics, Mittal et al. [41] realized the quadrupole TI based on silicon ring resonators (Fig. 3b) with judiciously tailored couplings between on-site and link resonators such that the total per-cell Berry flux and topological charge were  $\pi$  and nought, respectively. The quadrupole moment of the bulk is quantized due to the presence of the reflection symmetries in the lattice [40]. In the topologically non-trivial regime, when the inter-cell coupling strength exceeds intra-cell one, there appear gapped edge dipole states, which in their turn represent boundary TIs. Corners, being spatial defects for topologically nontrivial

polarization states, form the zero-dimensional boundary of the 1D lattice boundary and host localized topological modes which belong simultaneously to the two adjacent edges.

The topological invariants and quantized multipole moments can be calculated using the nested Wilson loop approach. Wilson loops represent generalization of the one-dimensional Berry phase and are connected to the eigenvalues of the position operator, thus to the generalisation of the problem of polarisation in solids [40]. To describe higher-order topology, it is instructive to define a Wilson loop operator and construct Wannier Hamiltonian for each boundary. The original space of energy bands, which can be degenerate at some high-symmetry points of the Brillouin zone, is split into single-band subspaces by picking out Wannier band subsets. Despite being gapped, the Wannier bands can still possess their own topological invariants which are calculated from the nested Wilson loops' behavior. This technique is applied to evaluate the polarization of a boundary and quantised corner charges.

Higher-order topological insulators without quantized multipole moments are known as crystalline topological insulators. They are characterized by fractional quantized bulk dipole polarization [43]. Such higher-order TIs are easier to implement in subwavelength photonics, as they do not require the coexisting positive and negative couplings [44, 45].

The corner states deduced from the model lattice Hamiltonians with nearest-neighbour interactions are conventional for condensed matter systems. But, in photonic systems, long-range interactions cannot be neglected that may lead to the emergence of specific corner modes dubbed as type-II [46].

**Topological lasing.** Other important distinction of topological photonic systems from their Hermitian quantum counterparts include the presence of absorption/radiation losses [47] or, conversely, optical gain. As such, active topological cavities hold special promise for a design of lasers. One of the cornerstone ideas is to employ a topologically protected mode as a lasing mode. By this means, lasing process is expected to become immune to perturbations of the system, such as local deformations of a cavity. The first examples of topological lasers were 1D inspired by the non-Hermitian SSH model described in [48]. The predictions of that model were observed in a trio of experiments: in a zigzag polariton lattice of micropillars [49], and ring resonator lattices with embedded InGaAsP/InP quantum wells [50, 51]. Uniform pumping results in spatially delocalized multimode emission due to competition between bulk modes, while pumping a single sublattice results in



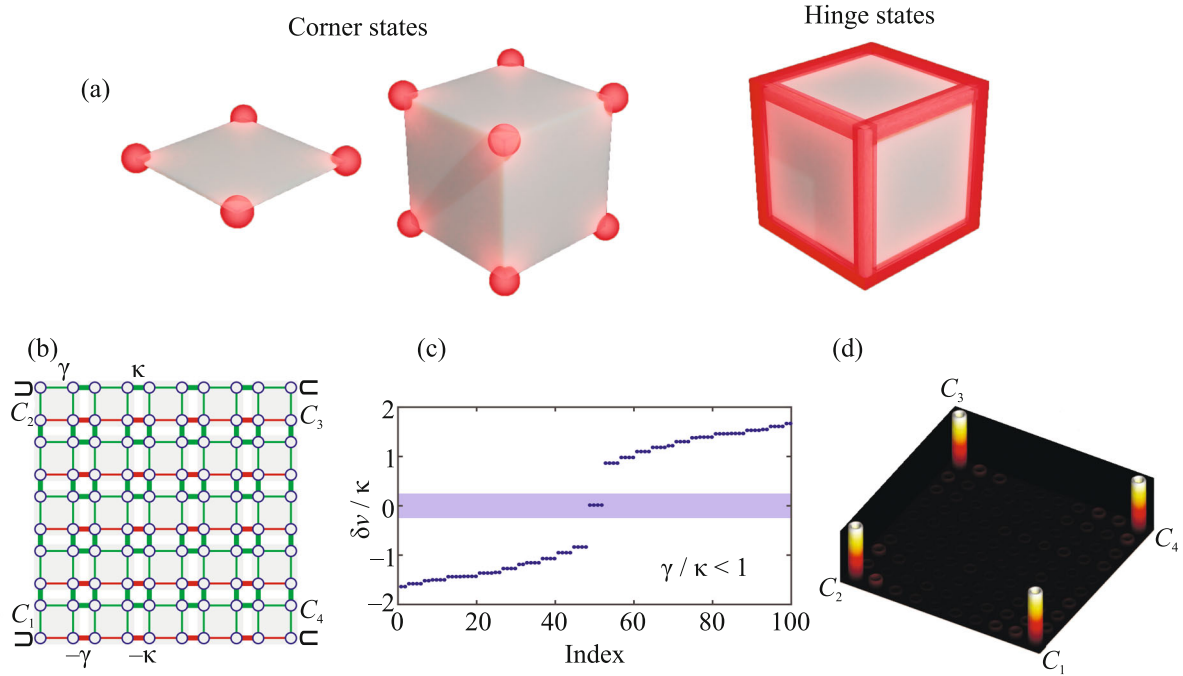


Fig. 3. (Color online) (a) – Corner and hinge states are the characteristic representatives of generalized bulk-boundary correspondence relating multipole moments in  $N$ -dimensional bulk to the quantized charge/current carried by lower-dimensional sub-spaces of bulk boundaries, i.e., with dimensionality reduced by more than one order. (b) – Schematic of the 2D lattice with quantized bulk quadrupole moment. Thick (thin) lines connecting lattice sites (circles) illustrate strong (weak) coupling strengths and their color indicates positive (green) and negative (red) sign of couplings ordered in the way that the net gauge equal to  $\pi$  threads each unit cell. (c) – Provided the inter-cell coupling exceeds the intra-cell one, the lattice exhibits the quadrupolar topological phase and hosts zero-energy four-fold degenerate states in the corners. (d) – Experimentally measured spatial intensity profiles of localized corner modes in topologically non-trivial lattice of silicon ring resonators [41]. Adapted from [41]

single mode lasing of the topological interface state as long as the bulk bandgap remains open. Later, a topological laser was realized in a two-dimensional array of micro-ring resonators with special coupling between the rings designed to follow a topological model so that it supports topological edge states. It was shown that a pump localized to the edge sites is required to suppress bulk mode lasing and induce stable single mode lasing of the edge states [52]. For comparison, in similar non-topological models, disorder tends to induce mode localization, resulting in multi-mode lasing involving modes localized at different positions along the edge. Topological resilience helps to overcome Anderson localization along the edge, thus producing modes that do not localize and can lase coherently [53]. The slope efficiency can thus be improved compared to a simple linear array of lasers.

The concepts of topology may serve as a significant guiding scheme for the smart control of a number, spectral separation, localization scales and quality factors of edge, corner and defect modes in

topological cavities for lasing [8]. This scope underpins promising design principles in nanophotonics. Particular experimental implementations of active nanophotonic topological metasurfaces, shown in Fig. 4, are based on indium gallium arsenide phosphide (InGaAsP) membranes incorporating quantum wells that act as a gain medium and serve as an internal light probe in the near infrared [54, 55]. The metasurfaces were fabricated using electron-beam lithography and subsequent dry and wet etching to suspend a membrane. The semiconductor slabs were nanopatterned to imprint the valley-Hall (Fig. 4, top row) and 2D SSH (Fig. 4, bottom row) lattices of air holes.

Figure 4a shows a small-scale triangle-shaped topological cavity based on the closed valley-Hall domain wall created by inversion of staggering the sizes of triangular air nanoholes in a bipartite honeycomb lattice. In the bandgap frequency range, the cavity supports a discrete spectrum of modes confined to the domain wall. Figures 4b, c show real-space emission profiles below and

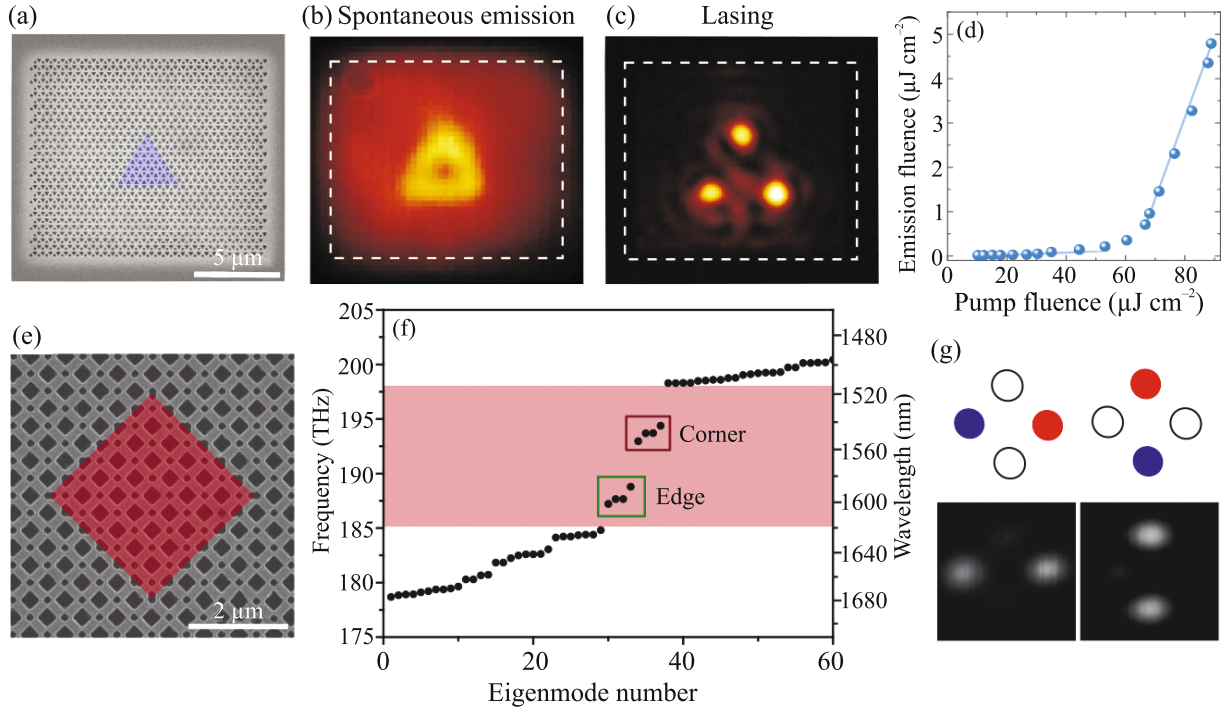


Fig. 4. (Color online) Lasing in nanophotonic topological cavities. (a) – SEM image of the fabricated sample. False-colour triangle shades the interior of the valley-Hall topological cavity. (b), (c) – Spatial distribution of emission for the pump intensity (b) below and (c) above the lasing threshold. (d) – Emission power vs. pump power showing a threshold transition to lasing. (e) – SEM image of the fabricated square-shaped cavity. (f) – The photonic bandgap of the infinite periodic structure opens in a wavelength range around 1550 nm and comprises 4 corner and 4 edge modes for bounded lattice. (g) – Dipolar lasing from coupled corner states: schematic visualization (top), measured mode images (bottom). Adapted from [54, 55]

above the lasing threshold. In the regime of spontaneous emission enhancement along the entire perimeter of the triangular cavity is associated with the edge states. When increasing a pump power, there occurs a threshold transition to lasing with a narrow linewidth, the emission gets confined at the three corners. This triade lasing mode emerges depending on the degree of asymmetry between two air holes.

The topological cavity in Fig. 4e contains a square-shaped domain wall separating nontrivial inner and trivial outer domains, created by inverting the order of smaller and larger distances between square air holes [55]. Given coupling of the corner states, four multipolar corner modes can be distinguished in the spectrum Fig. 4f, namely, the quadrupole, two degenerate dipoles, and the monopole. Photoluminescence measurements for the cavity were performed using a 980-nm pulsed pump laser at room temperature, and four lasing modes with different wavelengths were identified by employing hyperspectral imaging. The measured images of lasing modes were found to corroborate calculated electric-field intensity profiles of the corner-state modes (Fig. 4g). The multipolar corner-state lasing was

observed even when a defect was introduced at the interface between the trivial and nontrivial domains close to the corner.

**Outlook.** Topological photonics is likely to continue to be a highly active and flourishing area of research for the next decade. It proves itself not only useful for classical light control but also promising for a variety of quantum optical applications [56, 57]. Robustness and backscattering suppression offered by topological structures are paramount for the quantum optics, when each photon counts. Fabrication imperfections and scattering losses typical for the integrated photonics platform limit performance and scalability of such devices. Topological photonics can help to overcome these obstacles paving the way for robust quantum light sources and protected photon states on a chip. To date, several remarkable demonstrations have already been made, including topologically protected single-photon states [58, 59], correlated biphoton states [60–62], as well as topologically protected entangled photon states both for path- and time-bin-entanglement [63, 64]. We anticipate harnessing topological photonic phases in nonlinear and quantum op-



tics [8] will drive the cutting-edge developments in quantum technologies.

Links are being established between topological photonics and other frontier topics, including bound states in the continuum [65], structured light [66], and transformation optics. The high-quality-factor topological modes can be employed in nanolasers with superior stability, in the exotic manipulation of local optical heating for the purposes of optical nanothermometry [67] and hybrid polaritonic metasurfaces. For instance, it was proven that integration of InSe films with resonant photonic structures enables enhancing the quantum outcome of excitonic emitters in the former [68]. By integrating excitonic reservoirs with topological cavities, quantum emission can be tailored, directed and selectively generated with a specific handedness.

Intriguing opportunities also arise in the field of optical computing. It has been shown that the concepts of topological photonics can be applied for the purpose of achieving spatial differentiation in edge detection applications [69–71]. New advances can be expected at the intersection of topological physics with integrated photonic systems for optical neuromorphic computing [72]. It can open prospects for novel image processing devices with ultrafast operation speed and low energy consumption.

This work was supported by the Russian Science Foundation (Grant # 20-72-00148).

D.A. Smirnova thanks Y.S. Kivshar for the useful advice.

1. L. Lu, J. D. Joannopoulos, and M. Soljačić, *Nature Physics* **12**, 626 (2016).
2. M. Z. Hasan and C. L. Kane, *Rev. Mod. Phys.* **82**, 3045 (2010).
3. K. von Klitzing, T. Chakraborty, P. Kim, V. Madhavan, X. Dai, J. McIver, Y. Tokura, L. Savary, D. Smirnova, A. M. Rey, C. Felser, J. Gooth, and X. Qi, *Nature Reviews Physics* **2**, 397 (2020).
4. C. L. Kane and E. J. Mele, *Phys. Rev. Lett.* **95**, 146802 (2005).
5. D. J. Thouless, M. Kohmoto, M. P. Nightingale, and M. den Nijs, *Phys. Rev. Lett.* **49**, 405 (1982).
6. M. Kohmoto, *Ann. Phys.* **160**, 343 (1985).
7. T. Ozawa, H. M. Price, A. Amo, N. Goldman, M. Hafezi, L. Lu, M. C. Rechtsman, D. Schuster, J. Simon, O. Zilberberg, and I. Carusotto, *Rev. Mod. Phys.* **91**, 015006 (2019).
8. D. Smirnova, D. Leykam, Y. Chong, and Y. Kivshar, *Appl. Phys. Rev.* **7**, 021306 (2020).
9. J. Cayssol and J. N. Fuchs, *New J. Phys.* **4**, 034007 (2021).
10. F. Ghahari, D. Walkup, C. Gutiérrez, J. F. Rodríguez-Nieva, Y. Zhao, J. Wyrick, F. D. Natterer, W. G. Cullen, K. Watanabe, T. Taniguchi, L. S. Levitov, N. B. Zhitenev, and J. A. Strosio, *Science* **356**, 845 (2017).
11. E. Cohen, H. Larocque, F. Bouchard, F. Nejdassattari, Y. Gefen, and E. Karimi, *Nature Reviews Physics* **1**, 437 (2019).
12. B. Yang, Q. Guo, B. Tremain, R. Liu, L. E. Barr, Q. Yan, W. Gao, H. Liu, Y. Xiang, J. Chen, C. Fang, A. Hibbins, L. Lu, and S. Zhang, *Science* **359**, 1013 (2018).
13. L. Balents, *Physics* **4**, 36 (2011).
14. W. P. Su, J. R. Schrieffer, and A. J. Heeger, *Phys. Rev. Lett.* **42**, 1698 (1979).
15. N. Malkova, I. Hromada, X. Wang, G. Bryant, and Z. Chen, *Opt. Lett.* **34**, 1633 (2009).
16. A. P. Slobozhanyuk, A. N. Poddubny, A. E. Miroshnichenko, P. A. Belov, and Y. S. Kivshar, *Phys. Rev. Lett.* **114**, 123901 (2015).
17. A. B. Khanikaev and G. Shvets, *Nature Photon.* **11**, 763 (2017).
18. R. Roy, *Phys. Rev. B* **79**, 195322 (2009).
19. Y. Yang, Z. Gao, H. Xue, L. Zhang, M. He, Z. Yang, R. Singh, Y. Chong, B. Zhang, and H. Chen, *Nature* **565**, 622 (2019).
20. B. Yang, Q. Guo, B. Tremain, L. E. Barr, W. Gao, H. Liu, B. Béri, Y. Xiang, D. Fan, A. P. Hibbins, and S. Zhang, *Nat. Commun.* **8**, 1 (2017).
21. X. Wan, A. M. Turner, A. Vishwanath, and S. Y. Savrasov, *Phys. Rev. B* **83**, 205101 (2011).
22. M. Onoda, S. Murakami, and N. Nagaosa, *Phys. Rev. Lett.* **93**, 083901 (2004).
23. M. Zhou, L. Ying, L. Lu, L. Shi, J. Zi, and Z. Yu, *Nat. Commun.* **8**, 1388 (2017).
24. F. D. M. Haldane and S. Raghu, *Phys. Rev. Lett.* **100**, 013904 (2008).
25. S. Raghu and F. D. M. Haldane, *Phys. Rev. A* **78**, 033834 (2008).
26. Z. Wang, Y. D. Chong, J. D. Joannopoulos, and M. Soljačić, *Phys. Rev. Lett.* **100**, 013905 (2008).
27. Z. Wang, Y. Chong, J. D. Joannopoulos, and M. Soljačić, *Nature* **461**, 772 (2009).
28. M. Hafezi, S. Mittal, J. Fan, A. Migdall, and J. M. Taylor, *Nature Photon.* **7**, 1001 (2013).
29. M. C. Rechtsman, J. M. Zeuner, Y. Plotnik, Y. Lumer, D. Podolsky, F. Dreisow, S. Nolte, M. Segev, and A. Szameit, *Nature* **496**, 196 (2013).
30. D. Smirnova, S. Kruk, D. Leykam, E. Melik-Gaykazyan, D.-Y. Choi, and Y. Kivshar, *Phys. Rev. Lett.* **123**, 103901 (2019).
31. A. Serdyukov, I. Semchenko, S. Tretyakov, and A. Sihvola, *Electromagnetics of bi-anisotropic materials: Theory and applications*, Gordon & Breach Science Publishers, Amsterdam (2001).

32. A. B. Khanikaev, S. H. Mousavi, W.-K. Tse, M. Kargarian, A. H. MacDonald, and G. Shvets, *Nature Mater.* **12**, 233 (2013).
33. R. Alaee, M. Albooyeh, A. Rahimzadegan, M. S. Mirmoosa, Y. S. Kivshar, and C. Rockstuhl, *Phys. Rev. B* **92**, 245130 (2015).
34. A. P. Slobozhanyuk, A. B. Khanikaev, D. S. Filonov, D. A. Smirnova, A. E. Miroschnichenko, and Y. S. Kivshar, *Sci. Rep.* **6**, 22270 (2016).
35. A. Slobozhanyuk, S. H. Mousavi, X. Ni, D. Smirnova, Y. S. Kivshar, and A. B. Khanikaev, *Nature Photon.* **11**, 130 (2017).
36. D. A. Bobylev, D. A. Smirnova, and M. A. Gorlach, *Laser Photonics Rev.* **15**, 1900392 (2020).
37. X. Ni, D. Purtseladze, D. A. Smirnova, A. Slobozhanyuk, A. Alù, and A. B. Khanikaev, *Sci. Adv.* **4**, eaap8802 (2018).
38. R. D. King-Smith and D. Vanderbilt, *Phys. Rev. B* **47**, 1651 (1993).
39. D. Vanderbilt and R. D. King-Smith, *Phys. Rev. B* **48**, 4442 (1993).
40. W. A. Benalcazar, B. A. Bernevig, and T. L. Hughes, *Science* **357**, 61 (2017).
41. S. Mittal, V. V. Orre, G. Zhu, M. A. Gorlach, A. Poddubny, and M. Hafezi, *Nature Photon.* **13**, 692 (2019).
42. C. W. Peterson, W. A. Benalcazar, T. L. Hughes, and G. Bahl, *Nature* **555**, 346 (2018).
43. W. A. Benalcazar, T. Li, and T. L. Hughes, *Phys. Rev. B* **99**, 245151 (2019).
44. F. Liu and K. Wakabayashi, *Phys. Rev. Lett.* **118**, 076803 (2017).
45. B.-Y. Xie, G.-X. Su, H.-F. Wang, H. Su, X.-P. Shen, P. Zhan, M.-H. Lu, Z.-L. Wang, and Y.-F. Chen, *Phys. Rev. Lett.* **122**, 233903 (2019).
46. M. Li, D. Zhirihin, M. Gorlach, X. Ni, D. Filonov, A. Slobozhanyuk, A. Alù, and A. B. Khanikaev, *Nature Photon.* **14**, 89 (2020).
47. D. Leykam and D. A. Smirnova, *Nature Physics* **17**, 632 (2021).
48. H. Schomerus, *Opt. Lett.* **38**, 1912 (2013).
49. P. St-Jean, V. Goblot, E. Galopin, A. Lemaitre, T. Ozawa, L. L. Gratiet, I. Sagnes, J. Bloch, and A. Amo, *Nature Photon.* **11**, 651 (2017).
50. M. Parto, S. Wittek, H. Hodaei, G. Harari, M. A. Bandres, J. Ren, M. C. Rechtsman, M. Segev, D. N. Christodoulides, and M. Khajavikhan, *Phys. Rev. Lett.* **120**, 113901 (2018).
51. H. Zhao, P. Miao, M. H. Teimourpour, S. Malzard, R. El-Ganainy, H. Schomerus, and L. Feng, *Nat. Commun.* **9**, 981 (2018).
52. M. A. Bandres, S. Wittek, G. Harari, M. Parto, J. Ren, M. Segev, D. N. Christodoulides, and M. Khajavikhan, *Science* **359**, eaar4005 (2018).
53. G. Harari, M. A. Bandres, Y. Lumer, M. C. Rechtsman, Y. D. Chong, M. Khajavikhan, D. N. Christodoulides, and M. Segev, *Science* **359**, eaar4003 (2018).
54. D. Smirnova, A. Tripathi, S. Kruk, M.-S. Hwang, H.-R. Kim, H.-G. Park, and Y. Kivshar, *Light Sci. Appl.* **9**, 127 (2020).
55. H.-R. Kim, M.-S. Hwang, D. Smirnova, K.-Y. Jeong, Y. Kivshar, and H.-G. Park, *Nat. Commun.* **11**, 5758 (2020).
56. A. Blanco-Redondo, *Proc. IEEE* **108**, 837 (2020).
57. Q. Yan, X. Hu, Y. Fu, C. Lu, C. Fan, Q. Liu, X. Feng, Q. Sun, and Q. Gong, *Adv. Opt. Mater.* **9**, 2001739 (2021).
58. T. Kitagawa, M. A. Broome, A. Fedrizzi, M. S. Rudner, E. Berg, I. Kassal, A. Aspuru-Guzik, E. Demler, and A. G. White, *Nat. Commun.* **3**, 1 (2012).
59. S. Barik, A. Karasahin, C. Flower, T. Cai, H. Miyake, W. DeGottardi, M. Hafezi, and E. Waks, *Science* **359**, 666 (2018).
60. A. Blanco-Redondo, B. Bell, D. Oren, B. J. Eggleton, and M. Segev, *Science* **362**, 568 (2018).
61. S. Mittal, E. A. Goldschmidt, and M. Hafezi, *Nature* **561**, 502 (2018).
62. Y. Wang, X.-L. Pang, Y.-H. Lu, J. Gao, Y.-J. Chang, L.-F. Qiao, Z.-Q. Jiao, H. Tang, and X.-M. Jin, *Optica* **6**, 955 (2019).
63. S. Mittal, V. V. Orre, and M. Hafezi, *Opt. Express* **24**, 15631 (2016).
64. M. Wang, C. Doyle, B. Bell, M. J. Collins, E. Magi, B. J. Eggleton, M. Segev, and A. Blanco-Redondo, *Nanophotonics* **8**, 1327 (2019).
65. P. Tonkaev and Y. Kivshar, *JETP Lett.* **112**, 615 (2020).
66. A. Forbes, M. de Oliveira, and M. R. Dennis, *Nature Photon.* **15**, 253 (2021).
67. G. P. Zograf, Y. F. Yu, K. V. Baryshnikova, A. I. Kuznetsov, and S. V. Makarov, *JETP Lett.* **107**, 699 (2018).
68. A. D. Gartman, M. K. Kroychuk, A. S. Shorokhov, and A. A. Fedyanin, *JETP Lett.* **112**, 233903 (2020).
69. W. Zhang and X. Zhang, *Phys. Rev. Appl.* **11**, 054033 (2019).
70. T. Zhu, Y. Lou, Y. Zhou, J. Zhang, J. Huang, Y. Li, H. Luo, S. Wen, S. Zhu, Q. Gong, M. Qiu, and Z. Ruan, *Phys. Rev. Appl.* **11**, 034043 (2019).
71. T. Zhu, C. Guo, J. Huang, H. Wang, M. Orenstein, Z. Ruan, and S. Fan, *Nat. Commun.* **12**, 680 (2021).
72. D. T. H. Tan, *Adv. Photonics Res.* **9**, 2100010 (2021).